SpezialForschungsBereich F 32

Karl–Franzens Universität Graz
Technische Universität Graz
Medizinische Universität Graz

The effect of receiver coil orientations on the imaging performance of magnetic induction tomography

Doğa Gürsoy Hermann Scharfetter

SFB-Report No. 2009–042 September 2009

A–8010 GRAZ, HEINRICHSTRASSE 36, AUSTRIA

Supported by the
Austrian Science Fund (FWF)

Der Wissenschaftsfonds.

SFB sponsors:

- **Austrian Science Fund** (FWF)
- **University of Graz**
- **Graz University of Technology**
- **Medical University of Graz**
- **Government of Styria**
- **City of Graz**

The effect of receiver coil orientations on the imaging performance of magnetic induction tomography

D Gürsoy and H Scharfetter

September 1, 2009

Abstract

Magnetic induction tomography is an imaging modality which aims to reconstruct the conductivity distribution of the human body. It uses magnetic induction to excite the body and an array of sensor coils to detect the perturbations in the magnetic field. Up to now, much effort has been expended with the aim of finding an efficient coil configuration to extend the dynamic range of the measured signal. However, the merits of different sensor orientations on the imaging performance have not been studied in great detail so far. Therefore, the aim of the study is to fill the void of a systematic investigation of coil orientations on the reconstruction quality of the designs. To this end, a number of alternative receiver array designs with different coil orientations were suggested and the evaluations of the designs were performed based on the singular value decomposition. A generalized class of quality measures, the subclasses of which are linked to both the spatial resolution and uncertainty, was used to assess the performance on the radial and axial axes of a cylindrical phantom. The detectability of local conductivity perturbations in the phantom was explored using the reconstructed images. It is possible to draw the conclusion that the proper choice of the coil orientations significantly influences the number of usable singular vectors and accordingly, the stability of image reconstruction, although the effect of increased stability on the quality of the reconstructed images was not of paramount importance due to the reduced independent information content of the associated singular vectors.

Keywords: Magnetic induction tomography, coil optimization, image reconstruction

[1]D. Gürsoy and H. Scharfetter are with the Institute of Medical Engineering, Graz University of Technology, Austria. e-mail: guersoy@tugraz.at

[2]This work was supported by the SFB project F32-N18 granted by the Austrian Science Fund and published in IOP Meas. Sci. Technol.

1 Introduction

Magnetic induction tomography (MIT) is a noninvasive and contactless imaging modality which aims to reconstruct the electrical conductivity distribution of the human body [1]–[7]. An eddy current density is generated via magnetic induction using the transmitter coils and the changes in the magnetic field due to the conductivity perturbations within the body are recorded by an array of receiver coils. The corresponding inverse problem for the conductivity reconstruction is severely ill-posed and the regularization methods are widely applied to overcome the ill-posedness [8]–[10]. The common approach for the inversion is to seek minimum L_2-norm solutions by algorithms which use the linearized forward operators, however, other approaches such as the level-set type methods were also suggested [11].

In MIT, the change in the magnetic field due to the conductivity perturbation is much weaker than the primary magnetic field which leads to a narrow dynamic range in the receiver channels. Up to now, much effort has been expended with the aim of reaching an efficient coil configuration to extend the dynamic range of the measured signal. For this purpose, flux cancellation techniques like back off coils [12], specially oriented sensors [13]–[15], and gradiometers realized on printed circuit boards (PCB) [16]–[17] or as coils [18] have been extensively analyzed. However, the merits of different sensor orientations on the imaging performance have not been studied in great detail so far. Therefore, the goal of this paper is to fill the void of a systematic investigation of the coil orientations on the reconstruction quality of the designs.

In this study, a number of alternative receiver array designs with different coil orientations were suggested and the evaluation of the designs were performed based on the singular value decomposition (SVD) assuming that the underlying model is linear. The image resolution and variance measures were used to analyze the performance on the radial and axial axes of a cylindrical phantom and a class of quality measures, the subclasses of which are linked to these measures, i.e., spatial resolution and image uncertainty, was used to assess the overall performance of the designs. The detectability of three different local conductivity perturbations in the phantom was investigated using the reconstructed images for noisy and noise-free data.

2 Methods

2.1 Simulation of the voltage data

To acquire the induced voltage data in the receiver coils, the computation of the electric field produced by an energized coil in the proximity of a volume conductor is needed. According to the reciprocity theorem [19], the corresponding expression for data simulation is as follows,

$$v = \int_{\Omega} (\kappa \mathbf{E}_d) \cdot \mathbf{E}_a d\Omega \tag{1}$$

where $\kappa = \sigma + jw\epsilon$ is the admittivity of the body and Ω is the body volume. $\mathbf{E}_d$ is the direct electric field due to the transmitter coils and $\mathbf{E}_a$ is the adjoint electric field within the body assuming unity excitations in the receiver coils as if they were acting as transmitters. By using (1), one can generate a maximum number of $i \times j$ complex valued independent data assuming i transmitters and j receivers.

For the computation of the electric field, as auxiliary potentials, the electric scalar potential ϕ and the magnetic vector potential $\mathbf{A}$ were used and the expression is given as,

$$\mathbf{E} = -\nabla\phi - jw\mathbf{A} \tag{2}$$

where w is the operating frequency of the excitation field. For medical MIT, it is usually assumed that the contribution of the secondary magnetic field to the computation of the induced currents to be negligible [20]. This results in decoupling of the potential equations and the magnetic vector potential in the absence of the volume conductor [21] is used directly as a source term for the computation of the electric potential. The governing partial differential equations for the solution of the scalar electric potential within the body are,

$$\nabla \cdot \kappa\nabla\phi = -jw\mathbf{A} \cdot \nabla\kappa \quad \in \Omega \tag{3}$$

$$\nabla\phi \cdot \mathbf{n} = -jw\mathbf{A} \cdot \mathbf{n} \quad \in \partial\Omega \tag{4}$$

by defining $\mathbf{n}$ as the normal vector directed outward from the body surface. For the solution of ϕ, the body was meshed using first order tetrahedrons and a piecewise constant κ within the body was assumed by assigning constant conductivity and permittivity values to each voxel. The finite element method was used to obtain the system of equations and the inverse preconditioned quasi-minimal residual method was used for the solution [22].

The data acquired from eq1 are complex valued and consist of in-phase and quadrature components with respect to the primary excitation. For medical MIT, in-phase and quadrature components can be independently used to reconstruct the conductivity and permittivity images, respectively. However, reconstruction of the permittivity distribution currently seems infeasible due to some technical limitations [23], therefore, this paper will only focus on conductivity imaging using the real part of the voltage data.

2.2 Image reconstruction

Let the relation between the real part of the voltage data and the conductivity be expressed as, $v = \psi(\sigma)$, where ψ is a nonlinear function acting on a given conductivity, σ. The corresponding inverse problem, $\sigma = \psi^{-1}(v)$, is severely ill-posed. The most commonly used approach to address this problem is to assume linearity and solve for the small perturbations around a reference conductivity distribution. Thus, for a feasible reconstruction, the awareness of the expected solution (in other words, a good initialization) is essential to cope with the difficulties related to nonlinearity.

By using (1), the sensitivity of the data to the conductivity perturbations can be approximated as,

$$\frac{\partial v}{\partial \sigma} = \frac{1}{\Delta\sigma}\int_{\Omega}(\Delta\sigma \mathbf{E}_d)\cdot\mathbf{E}_a d\Omega \tag{5}$$

where $\Delta\sigma$ denotes the conductivity deviations from a reference distribution. Therefore, assuming admissible conductivity fluctuations, by using (5), the following system of linear equations can be formed,

$$\mathbf{S}\Delta\sigma = \Delta v \tag{6}$$

where $\mathbf{S}$ is referred to as the sensitivity matrix. Each row corresponds to one transmit-receive coil pair and each column to one voxel. Within the range of linearity, a fairly convenient solution for $\Delta\sigma$ can be obtained by minimizing the L_2-norm of the residuals between the measured and the estimated data. By defining $\mathbf{S}^{\dagger}$ as the pseudoinverse of $\mathbf{S}$, the solution can be obtained from,

$$\Delta\sigma = \mathbf{S}^{\dagger}\Delta v \tag{7}$$

By expressing SVD of $\mathbf{S}$ as $\mathbf{U}\Sigma\mathbf{V}^T$, where $\mathbf{U} = [\mathbf{u}_1, \mathbf{u}_2, \ldots, \mathbf{u}_m] \in R^{m\times m}$ and $\mathbf{V} = [\mathbf{v}_1, \mathbf{v}_2, \ldots, \mathbf{v}_n] \in R^{n\times n}$ are the singular vectors which form a basis for the data and the model space, respectively, and Σ is a diagonal matrix, the diagonal entries of which are called the singular values, $\mathbf{S}^{\dagger}$ can be computed from $\mathbf{V}\Sigma^{\dagger}\mathbf{U}^T$ where $\Sigma^{\dagger}$ is the pseudoinverse of Σ with every nonzero entry replaced by its reciprocal. Due to the ill-conditioning of $\mathbf{S}$, a truncation by using only the t column vectors of $\mathbf{U}$ and $\mathbf{V}$ corresponding to the t largest singular values is preferred to stabilize the inversion when the data are inaccurate. Therefore, the solution can be computed from,

$$\Delta\sigma = \mathbf{V}\Sigma_t^{\dagger}\mathbf{U}^T\Delta v \tag{8}$$

where the subscript t defines the truncation level that determines the stability of the inversion by ignoring the $n - t$ number of small singular values in Σ. Let ρ_1 be the largest singular value and ρ_k as the k^{th} largest one, the proper selection of the truncation level k, was established by choosing the maximum k that satisfies the following equality,

$$SNR = 20\log_{10}\left(\frac{\Delta v_{rms}}{\delta_{rms}}\right) \geq 20\log_{10}\left(\frac{\rho_1}{\rho_k}\right) \tag{9}$$

where Δv_{rms} and δ_{rms} are the root mean square of the perturbed voltage signal and the noise signal, respectively. The left hand side of the inequality is defined as the signal to noise ratio (SNR). In this paper, the noise was modeled as an additive white Gaussian noise of zero mean. Therefore, δ_{rms} denotes the standard deviation of the noise.

2.3 Evaluation of the designs

SVD of the sensitivity matrix was used to obtain a generalized class of quality measures which serves as a basis for the evaluation [24]. It is possible to quantify the image resolution and uncertainty by selecting particular subclasses of this measure (refer to appendix for details). Usually, the desired measure shall focus into a region, e.g. a slice or a single voxel, instead of the whole conductive domain, the effect of the singular vectors that span the parameters within that region must be computed. Let $\mathbf{F} = [\mathbf{f}_1, \mathbf{f}_2, \ldots, \mathbf{f}_k] \in R^{n \times k}$ be an arbitrary collection of the basis vectors for the desired region, denoted as F. The projection of the singular vectors onto F is written as,

$$\eta_j = \left(\sum_{i=1}^{k} (\mathbf{v}_j \cdot \mathbf{f}_i)^2 \right)^{1/2} \qquad j = 1, 2, \ldots, n \tag{10}$$

where $\mathbf{p} = [\eta_1, \eta_2, \ldots, \eta_n]^T \in R^{n \times 1}$ is defined as the projection vector. This vector denotes the effective singular vectors for F. For computational convenience, a natural and simple way to select the basis for F is using the unit vectors oriented parallel to each of the model parameter axes and defined as follows,

$$\mathbf{F}_{ij} = \begin{cases} 1, & \text{if } i = j \\ 0, & \text{if } i \neq j \end{cases} \tag{11}$$

By imposing that the singular values apply a weighting to the associated singular vectors, a set of quality measures for the region F can be defined as follows,

$$q_F(\alpha, t) = \begin{cases} \mathbf{p}^T \Sigma_t^{\alpha} \mathbf{p}, & \text{if } \alpha \geq 0 \\ \mathbf{p}^T \left(\Sigma_t^{\dagger} \right)^{|\alpha|} \mathbf{p}, & \text{if } \alpha < 0 \end{cases} \tag{12}$$

where α can be thought as an arbitrary weighting parameter and t is the truncation index. The resolution and uncertainty measures are the subset of the measure given by eq12, with α taking values of 0 and -2, respectively (see appendix). In these two particular cases, the resolution and uncertainty measures are equivalent to summing the diagonal elements of the model resolution matrix and the model covariance matrix, respectively, which corresponds to the voxels within F.

The selection of the α parameter in eq12 allows us to define a weighting between the resolution and the variance of the reconstructions and serves a useful base for design optimization. Different α values determines the effect of the singular values on the imaging performance. A positive α value tends to increase the effect of the larger singular values than the smaller ones so that the inversion would be better constrained under low levels of SNR. Since the number of the effective singular vectors is too little as compared to the unknown parameters, a positive weighting is more appropriate for MIT so that the effect of the smaller singular values are comparably reduced and the importance of the larger ones are raised.

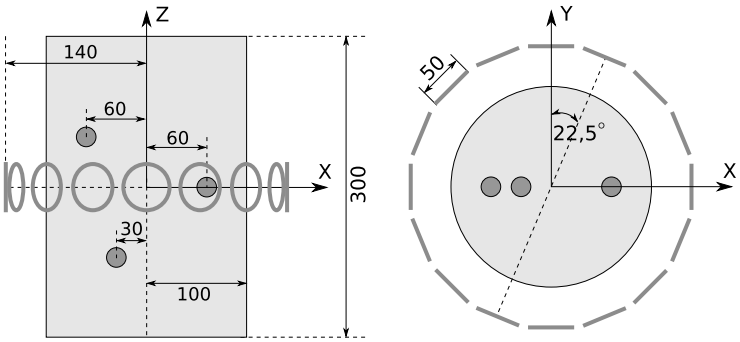

Figure 1: The cylindrical phantom and the positioning of the transmitter coils. The left and the right diagrams correspond to the side view and the top view. All units are given in millimetres.

Using eq12, the effect of the truncation level on the quality can be expressed as,

$$(\%)\,\Delta q_F(\alpha, t) = 100 \times \left(1 - \frac{q_F(\alpha, t)}{q_F(\alpha, t_{max})}\right) \tag{13}$$

where Δq_F is defined as the quality reduction in percentage due to the truncation. Considering the designs in this paper, $t_{max} = 256$ which denotes zero truncation.

2.4 Simulation setup

Six different designs with a fixed number of coils were compared and the goal was to assess the characteristics of the receiver coil orientations in terms of the measures applied. For excitation, 16 identical solenoid transmit coils with 25 mm radius were used with their centers uniformly positioned on a circular ring of 140 mm radius (see, figure 1). 16 receiver coils with 25 mm radius were placed with their centers on an inner ring of 130 mm radius. The designs differed by the receiver coil orientations where the unit vector along the coil axis was allowed to point in one of the three standard cylindrical coordinate basis vectors, $\mathbf{u}_\rho$, $\mathbf{u}_\varphi$ or $\mathbf{u}_z$. The designs are shown in figure 2 and are denoted as $D1$ ($\mathbf{u}_\rho$), $D2$ ($\mathbf{u}_\varphi$), $D3$ ($\mathbf{u}_z$), $D4$ ($\mathbf{u}_\rho$ and $\mathbf{u}_z$ alternating), $D5$ ($\mathbf{u}_\rho$ and $\mathbf{u}_\varphi$ alternating) and $D6$ ($\mathbf{u}_\varphi$ and $\mathbf{u}_z$ alternating).

A cylindrical phantom of 100 mm radius and 300 mm height with three local spherical inhomogeneities inside was used to test the imaging performance of the designs. The inhomogeneities had comparatively small radii of 10 mm so as to reflect in the images approximately the point spread functions at the locations [-60, 0, 50], [60, 0, 0] and [-30, 0, -70] mm.

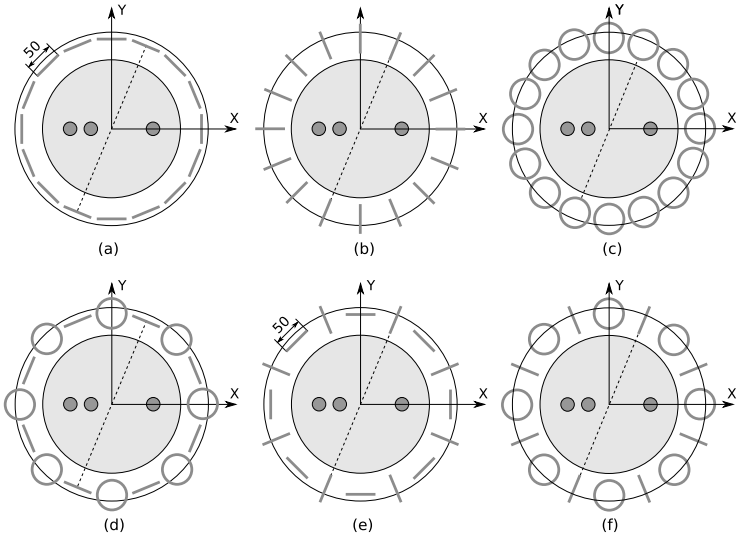

Figure 2: Demonstration of the receiver coil designs: (a) $D1$, (b) $D2$, (c) $D3$, (d) $D4$, (e) $D5$ and (f) $D6$.

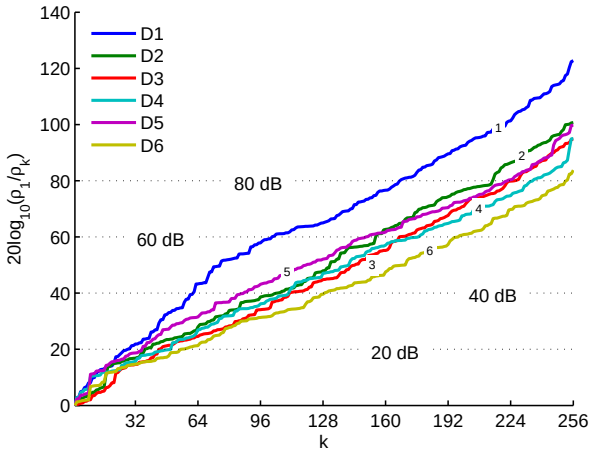

Figure 3: The logarithmic ratio between the first and the k^{th} singular value as compared to the SNR.

Table 1: Optimum truncation levels for the designs corresponding to different SNR levels. (-) means no truncation is necessary.

Design	20 dB	40 dB	60 dB	80 dB	100 dB
$D1$	28	62	102	168	222
$D2$	37	105	155	215	253
$D3$	44	111	167	227	–
$D4$	51	111	177	236	–
$D5$	36	88	150	223	–
$D6$	56	129	198	253	–

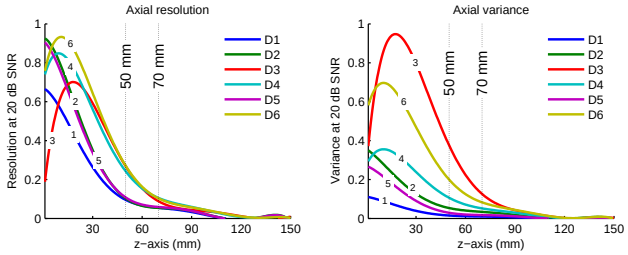

Figure 4: The curves of the normalized resolution and variance measures at 20 dB SNR level along the z-axis corresponding to the designs. The slices at 50 and 70 mm on the z-axis were marked as dotted vertical lines to highlight the locations of the perturbations. On the y-axes, 0 and 1 indicates the minimum and the maximum, respectively.

3 Results

The sensitivity matrices of the designs were computed using a uniform conductivity distribution within the phantom and the SVD was performed on the matrices. To determine the truncation level needed for a stable image reconstruction, the logarithmic ratios between the first and the remaining singular values as compared to the SNR levels were examined as in figure 3. The obtained truncation levels for the designs corresponding to several SNR levels are given in table 1. The curve corresponding to *D1* ascends more steeply than for all other designs, thus reflecting a faster drop of the singular values. For instance, only 28 singular values can be effectively used for image reconstruction considering 20 dB SNR. On the other hand, the curve of *D6* ascended with a more gentle slope and the corresponding truncation index was significantly higher considering the feasible SNR levels of a typical MIT system.

For a detailed analysis, the phantom was divided into thin slices of 10 mm thickness along the z-axis. The axial resolution and uncertainty measures at 20 dB SNR level associated with each slice were computed based on eq12 by substituting the α values as 0 and -2, respectively, and the associated curves were plotted in figure 4. The truncation necessary for a stable inversion was

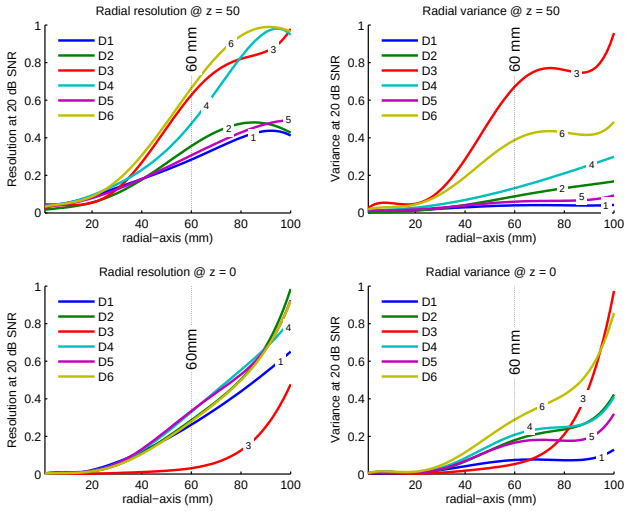

Figure 5: The curves of the normalized resolution and variance measures at 20 dB SNR level along the radial-axis considering different slices. The radial position at 60 mm was marked as a dotted vertical line on the radial-axis to highlight the locations of the perturbations. On the y-axes, 0 and 1 indicates the minimum and the maximum, respectively.

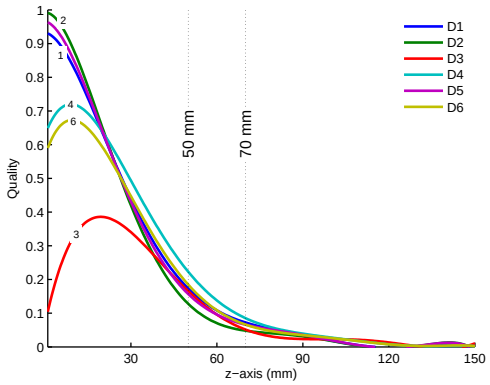

Figure 6: The normalized quality curves along the z-axis ($\alpha = 1$) corresponding to the designs. The slices at 50 and 70 mm on the z-axis were marked as dotted vertical lines to highlight the locations of the perturbations. On the y-axis, 0 and 1 indicates the minimum and the maximum, respectively.

obtained from table 1. Since the curves are symmetric with respect to the central plane, only the curves corresponding to the positive z-axis were plotted. The slices at 50 and 70 mm on the z-axis were marked as dotted vertical lines to highlight the locations of the perturbations. The curves of *D4* and *D6* showed the largest resolution among all designs except at the origin which represents the central slice. The peak of the curves of *D1*, *D2* and *D5* lie at the origin and they decay along the z-axis. In the variance plots, *D3* and *D6* showed the worst performance among all and *D1* was the most stable design with a low image variance.

For a radial analysis, transversal slices, i.e. at $z = 0$ and at $z = 50$ mm, were divided into tiny rings of different radii from the origin to the periphery of the slice. The thickness of the rings was selected as 10 mm. The corresponding curves of the resolution and variance measures at 20 dB SNR level along the radial-axis for two different slice positions were given in figure 5. The radial position at 60 mm was marked as a dotted vertical line on the radial-axis to label the location of the perturbation. *D3*, *D4* and *D6* showed better resolution in the off-central plane and considering the central plane, all designs showed comparably similar performances except *D3*, the resolution of which was significantly low. The plots for the slice at $z = 70$ mm showed similar curves as $z = 50$ mm and, thus, were not presented.

It is, in principle, not sufficient to investigate only the image resolution to compare the designs. For instance, some designs may show better resolution performances but the corresponding images might be unstable when the data are noisy. This shows the necessity of the overall performance measures as given in eq12. For the demonstration, a quality measure with a unity weight ($\alpha = 1$) was considered and the curves were plotted in figure 6. As noted from the plots,

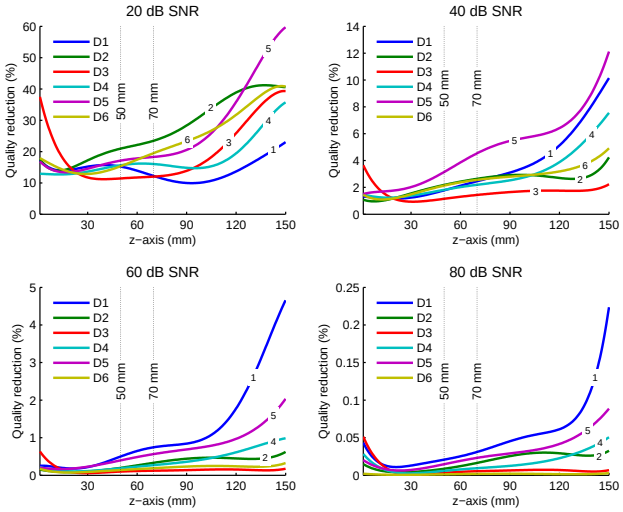

Figure 7: The effect of SNR on the design qualities of the designs ($\alpha = 1$). The slices at 50 and 70 mm on the z-axis were marked as dotted vertical lines to highlight the locations of the perturbation .

the quality of *D1*, *D2* and *D5* was significantly weighted for the central slice due to their low image variance. *D3* showed a very poor quality especially for the central slice and *D4* and *D6* showed fairly good results. Considering the slices beyond 20 mm, *D4* outperformed the other designs.

The effect of the truncation on the design quality was analyzed according to eq13 and the plots for several SNR levels were given in figure 7. With 60 dB and 80 dB SNR, *D1* has the largest reduction of quality compared to the other designs. This is probably due to the large number of neglected singular vectors. However, there is not a significant quality reduction of *D3* and *D6*. This scenario is different for low SNR levels. For 20 dB and 40 dB SNR, the qualities of *D2* and *D5*, respectively, drop rapidly, whereas, *D1* shows a moderate reduction for the associated SNR.

Reconstructed images of the designs from data without noise and with 20 dB noise are depicted for all designs in figure 8 and figure 9, respectively. The voltage data were simulated by changing the conductivity of the perturbations from 0.1 S/m to 0.2 S/m assuming a constant background conductivity of 0.1 S/m. The three transversal images were chosen to cut through the centers of the inhomogeneities. From the images, the perturbation located at [-30, 0, -70] mm was hardly recognizable and the depth sensitivity was found to be comparatively poor for all the designs. Perturbations close to the periphery appeared as bright spots but smeared out to large blobs according to their broad point spread functions. Due to the complete symmetry of the coil ring with respect to the median plane, the reconstruction algorithm could not distinguish between

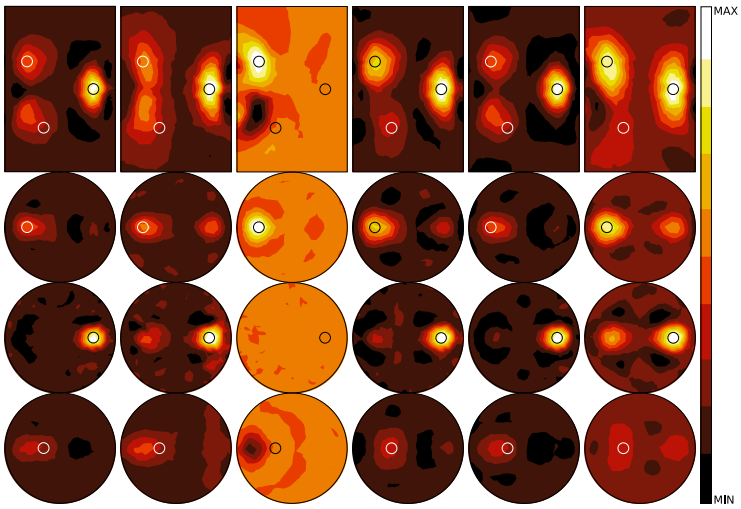

Figure 8: The images reconstructed from the corresponding designs using noise-free data. (a) D1, (b) D2, (c) D3, (d) D4, (e) D5 and (f) D6.

the perturbations which lie symmetric with respect to the symmetry plane. Thus, each perturbation off the median plane lead to an artificial mirror image in the opposite half space and the image intensity was reduced. The mirror artifacts completely cloak the deepest perturbation in all cases. The central slice was fairly well reconstructed in almost all designs except $D3$, which has no sensitivity at all to the median plane.

4 Discussions

The complete resolution analysis, i.e. examining, characterizing and reporting the PSF of each voxel, is very challenging due to the large number of parameters. Usually, some measures to quantify the key features of the PSFs are desired for evaluation. A recently proposed measure was the spread of the PSF quantified by the distance at which the function reaches a percentage of its maximum value [25]. However, this approach is not easily applicable for all locations due to the nonconvex and arbitrary shaped PSFs of MIT. Thus, in this work, we suggest to use only the peak values of the PSFs for quantification. This showed consistent and parallel results with the previously used evaluation of Merwa *et al* [25], since the peak value was found to be strictly dependent on the spread of the function, i.e., a high peak is an indicator of good resolution and low spread. Additionally, this measure is computationally much cheaper and robust.

The stability of the reconstructions, which addresses the possible artifacts arose from propagation of data errors into the imaging domain, has not been investigated much. In this work, the evaluation was carried out by a measure which was computed from the variances of the reconstructions due to an uncor-

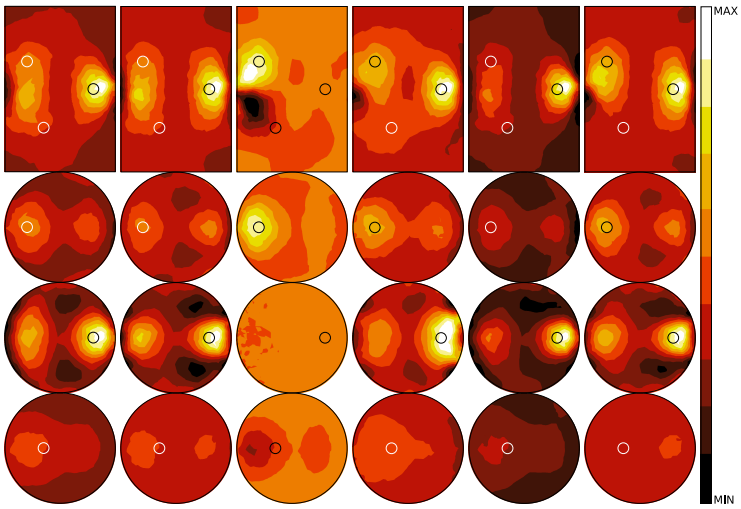

Figure 9: The images reconstructed from different designs using noisy data of 20 dB SNR. The truncation was applied according to table 2. (a) D1, (b) D2, (c) D3, (d) D4, (e) D5 and (f) D6.

related data noise. A clear trade-off between the resolution and the stability was noted. For instance, a decrease in the truncation level results in a more stable inversion by removing the effect of the smallest singular values, however, leads to a poorer resolution due to the reduction of the associated singular vectors. Considering these facts, we used a quality measure by which the resolution and the stability can be weighted accordingly. The motivation behind this weighting strategy can be inferred from figure 5 considering the slice at $z = 50$ mm. The designs $D4$ and $D6$ show similar characteristics in terms of resolution, however, the variance curve of $D6$ shows larger uncertainty in the image domain and, thus, the overall performance of $D6$ was concluded to be poorer than $D4$. This example shows the necessity of integrated approaches to quantify the performance to be used in design optimization.

As discussed in earlier publications [16], $\mathbf{u}_z$ directed coils (as $D3$) have nearly the same characteristics as the vertically positioned (on end rings) planar gradiometers with their main axis pointing towards $\mathbf{u}_\rho$. Similarly, it is also possible to construct analogous gradiometer designs. For instance, considering $D2$, it is possible to build an analogous design by using horizontally positioned (side by side rings) planar gradiometers pointing in direction $\mathbf{u}_\rho$. The simulations that were not shown in the paper revealed that the zero-flow gradiometer receiver design suggested by Scharfetter *et al* [17], do not resemble $D1$ as expected, but produce similar images like $D3$. This is thought to be due to the comparatively larger size of the gradiometers, since the voltage induced in the ring placed far from the surface is considerably lower than the closer ring. Therefore, the designs $D2$, $D3$ and $D6$ can be fully implemented using planar gradiometers

instead of coils.

The reconstruction algorithm could not distinguish between the conductivity perturbations which are placed symmetric with respect to the median plane due to the complete symmetry of the coil rings. This causes artificial mirror images in the opposite half space for the perturbations off the median plane. From figure 8, it was noted that the mirror artefacts were bound to be positive for the designs $D1$, $D2$ and $D5$, the coil axes of which point along the horizontal directions ($\mathbf{u}_\rho$ and $\mathbf{u}_\varphi$) and negative for $D3$ which is constructed by $\mathbf{u}_z$ oriented coils. Therefore, considering the designs $D4$, $D6$, which have both the vertically and horizontally oriented coils, the mirror artefacts were partly cancelled due to the different sign characteristics of the artefacts.

5 Conclusions

In this study, a number of receiver array designs with different coil orientations were suggested and SVD was used to serve as a basis for the analysis. The analysis requires that the relationship between the model parameters and the data can be linearized around a reference model. The resolution and the variance measures were computed using the sensitivity matrix and the feasibility of using a generalized quality measure was demonstrated to draw reliable conclusions on the offered designs. The images corresponding to the investigated designs were reconstructed by using the noise-free and noisy data to present the artefacts in the images. It was found that the proper choice of the coil orientations significantly influences the number of usable singular vectors; thus, the stability of image reconstruction, although the effect of increased stability on the quality of the reconstructed images was not of paramount importance due to the reduced independent information content of the associated singular vectors. Each design has its own merits and shortcomings for different imaging regions and for different SNR levels, nevertheless, considering overall characteristics, *D1*, *D2* and *D5* found to be more focused to the median plane with high resolution and low image uncertainty. For the off-median regions, *D4* was found to be moderately better among others considering the practical noise levels of MIT, i.e., 20 to 40 dB.

6 Appendices

6.1 Image resolution and uncertainty

From the linear inverse theory, it is possible to obtain the theoretical resolution limits and the uncertainty of the reconstructions in terms of the sensitivity matrix. By using (6) and (7), the resolution matrix is given as follows,

$$\mathbf{R} = \mathbf{S}^\dagger \mathbf{S} \tag{14}$$

of which the columns are called the point spread functions and they represent the response of the system due to a point source. Ideally, when the resolution is

perfect, $\mathbf{R}$ is an identity matrix, however, due to the absent information that lies in the kernel of $\mathbf{S}$, $\mathbf{R}$ is significantly different from an identity matrix. Similarly, the model covariance matrix is written as,

$$\mathbf{C}_m = (\mathbf{S}^T \mathbf{C}_d \mathbf{S})^{-1} \tag{15}$$

where $\mathbf{C}_d$ is the data covariance matrix. Assuming that the data are uncorrelated and the data variances are normalized to unity, (A.1) and (A.2) can be expressed in terms of the SVD components as,

$$\mathbf{R} = \mathbf{V}\Sigma^{\dagger}\Sigma\mathbf{V}^T \tag{16}$$

$$\mathbf{C}_m = \mathbf{V}\Sigma^{\dagger}\Sigma^{\dagger}\mathbf{V}^T \tag{17}$$

Therefore, the resolution is simply $\mathbf{V}\mathbf{V}^T$ considering only the singular vectors corresponding to the nonzero singular values and the model covariance is the "weighted" version of the resolution matrix by the square of the associated singular values. From (A.3) and (A.4), it is clear that when the basis vectors for the region of interest is selected as in (11), the summation of the diagonal elements of $\mathbf{R}$ and $\mathbf{C}_m$ corresponding to the parameters of the focused region is equivalent to (12) for the α values of 0 and -2, respectively.

References

1 Griffiths H 2001 Magnetic Induction Tomography *Meas. Sci. Technol.* **12** 1126–31

2 Peyton A J 1996 An overview of electromagnetic inductance tomography: description of three different systems *Meas. Sci. Technol.* **7** 261–71

3 Scharfetter H, Lackner H K, and Rosell J 2001 Magnetic induction tomography: Hardware for multi-frequency measurements in biological tissues *Physiol. Meas.* **22** 131–46

4 Korjenevsky A, Cherepenin V and Sapetsky S 2000 Magnetic induction tomography: experimental realization *Physiol. Meas.* **21** 89-94

5 Scharfetter H, Köstinger A, and Issa S 2008 Hardware for quasi-single-shot multifrequency magnetic induction tomography (MIT): the Graz Mk2 system *Physiol. Meas.* **29** 431–43

6 Vauhkonen M, Hamsch M and Igney C H 2008 A measurement system and image reconstruction in magnetic induction tomography *Physiol. Meas.* **29** 445–54

7 Watson S, Williams R J, Gough W and Griffiths H 2008 A magnetic induction tomography system for samples with conductivities below 10 S m-1 *Meas. Sci. Technol.* **19** 045501

8 Hansen P 1998 *Rank-Deficient and Discrete Ill-Posed Problems* (Philadelphia: SIAM)

9 Merwa R, Hollaus K, Brunner P and Scharfetter H 2005 Solution of the inverse problem of magnetic induction tomography (MIT) *Physiol. Meas.* **26** 241–50

10 Soleimani M and Lionheart W R B 2006 Absolute Conductivity Reconstruction in Magnetic Induction Tomography Using a Nonlinear Method *IEEE Trans. Med. Imag.* **25** 1521–30

11 Soleimani M 2008 Computational aspects of low frequency electrical and electromagnetic tomography: A review study *Int. J. Num. Anal. Mod.* **5** 407–40

12 Griffiths H, Stewart W R, and Gough W 1999 Magnetic induction tomography: a measuring system for biological tissues *Ann. N Y Acad. Sci.* **873** 335–45

13 Igney C H, Watson S, Williams R J, Griffiths H, Dössel O 2005 Design and performance of a planar-array MIT system with normal sensor alignment *Physiol. Meas.* **26** 263–78

14 Watson S, Morris A, Williams R J, Griffiths H and Gough W 2004 A primary field compensation scheme for planar array magnetic induction tomography *Physiol. Meas.* **25** 271–9

15 Watson S, Igney C H, Dössel O, Williams R J and Griffiths H 2005 A comparison of sensors for minimizing the primary signal in planar-array magnetic induction tomography *Physiol. Meas.* **26** 319–31

16 Merwa R and Scharfetter H 2008 Magnetic induction tomography: comparison of the image quality using different types of receivers *Physiol. Meas.* **29** 417-29

17 Scharfetter H, Merwa R and Pilz K 2005 A new type of gradiometer for the receiving circuit of magnetic induction tomography (MIT) *Physiol. Meas.* **26** 307-1-8

18 Karbeyaz B Ü and Gençer N G 2003 Electrical conductivity imaging via contactless measurements: an experimental study *IEEE Trans. Med. Imag.* **22** 627–35

19 Mortarelli J R 1980 Generalization of the Geselowitz Relationship Useful in Impedance Plethysmographic Field Calculations *IEEE Trans. Biomed. Eng.* **27** 665–7

20 Gençer N G and Tek M N 1999 Electrical conductivity imaging via contactless measurements *IEEE Trans. Med. Imag.* **18** 617–27

21 Smythe W R 1965 *Static and dynamic electricity*, (New York: McGraw Hill) 290–1

22 Horesh L, Schweiger M, Bollhofer M, Douiri A, Holder D S and Arridge S R 2006 Multilevel preconditioning for 3D large scale soft field medical applications modeling *Int. J. Inf. Syst. Sci.* **2** 532–56

23 Scharfetter H, Casañas R and Rosell J 2003 Biological Tissue Characterization by Magnetic Induction Spectroscopy (MIS): Requirements and Limitations *IEEE Trans. Biomed. Eng.* **50** 870–80

24 Curtis A 1999 Optimal designs of focused experiments and surveys *Geophys. J. Int.* **139** 205–15

25 Merwa R and Scharfetter H 2007 Magnetic induction tomography: evaluation of the point spread function and analysis of resolution and image distortion *Physiol. Meas.* **28** 313-24